Article

On-Line Diagnostics of Electrolytic Capacitors in Fault-Tolerant LED Lighting Systems

Khaled Laadjal *, Fernando Bento * and Antonio J. Marques Cardoso *

CISE–Electromechatronic Systems Research Centre, University of Beira Interior, Calçada Fonte do Lameiro,
P–62001-001 Covilhã, Portugal
* Correspondence: laadjal.khaled1991@gmail.com (K.L.); fjfbento@ieee.org (F.B.);
ajmcardoso@ieee.org (A.J.M.C.)

Abstract: As technology advances, the utilization of lighting systems based on light-emitting diode (LED) technology is becoming increasingly essential, given its benefits in terms of efficiency, reliability, and lifespan. Unfortunately, the power electronic components required to drive LEDs are unable to compete with LED devices in terms of lifetime. Aluminum electrolytic capacitor (AEC) failures represent the root cause of power electronic equipment breakdown, mainly through both aging and temperature effects. This highlights the importance of designing robust power converter architectures and control methods that allow the evaluation of the condition of electrolytic capacitors while maintaining the performance of converter controllers, even in the presence of capacitor failure. On this basis, this work proposes a novel condition-monitoring system for the diagnosis of capacitor faults on a fault-tolerant LED driver, which is able to deal with the specific architecture and low ratings of the most recent LED lighting systems. The fault-detection task applies the short time least square Prony's (STLSP) approach to perform an online estimation of the ESR and C parameters, allowing the continuous evaluation of the electrolytic capacitor's condition and, as a result, the prevention of total system failure. With regard to capacitor failure, the experimental results suggest that the condition-monitoring task is extremely effective, even when considering a limited number of data samples.

Keywords: light-emitting diode (LED); electrolytic capacitors; equivalent series resistance (ESR); capacitance (C); Prony's method; fault-tolerant LED driver

1. Introduction

DC-link capacitors are key components of most power electronic converters. At the same time, these components also contribute significantly to the cost, size, and failure rate of converters [1]. Aluminum electrolytic capacitors (AECs) are the most common capacitors used in power electronics [2] because they can offer the highest energy density with the lowest cost. As a result, AECs are widely used in power electronic systems for energy storage and filtering applications [3]. AECs are among the most age-affected components in converters. About 30% of the failures in converters are caused by AECs, thus a major cause of breakdowns (Figure 1).

All the dominant failure mechanisms in capacitors cause an increase in the equivalent series resistance (ESR) and a decrease in capacitance (C). Generally, an increase in the ESR above 200% of its initial value and a decrease in capacitance below 80% of its initial value are considered signatures of failure [1,4]. The deterioration of AECs reduces a system's effectiveness and reliability [3]. Power electronic converters are an essential field for development in crucial applications such as renewable energy, electric vehicles, LED lighting, and many other safety-critical applications, as the demand for more efficient energy systems continues [4,5]. As a result of the increasing demand for power electronics,

reliable control and monitoring mechanisms are necessary to provide fault-tolerant operation in cases of component failure in these converters.
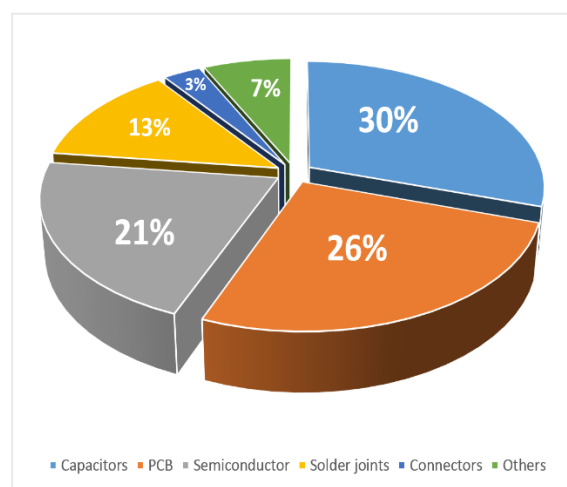

Figure 1. Failure-root-cause summary of power electronic systems.

The developments in LED technology have brought a host of different driver configurations, each with its own set of advantages. Increased efficiency benefits some topologies, whereas the addition of long-life capacitors improves the durability of other LED drivers [6]. Multiple LED driver designs are available, all of which are designed to suit the requirements and limitations imposed by applications such as indoor/outdoor lighting, automobiles, or greenhouses. LED drivers are frequently built and adjusted from basic AC-DC and/or DC-DC topologies to integrate functions such as precise power control or dimming. AC-DC LED drivers are frequently employed in applications that need AC power sources, such as indoor and outdoor illumination [7]. The growing interest in the adoption of DC microgrids [8] in homes and businesses necessitates the development of efficient and dependable power-conversion solutions. In this context, single-stage DC-DC converters are considered for LED lighting. The literature focuses on the improvement of the efficiency and power quality of, among other DC-DC conversion technologies, single-inductor multiple-output (SIMO) converters [9], interleaved flyback converters [10], resonant converters [11–13], and single-switch converters [14]. The majority of the converters described are intended to power many LED fixtures with a single power converter. To accomplish multiple output supply, multiple AECs are typically inserted in such LED drivers. None of the aforementioned LED drivers integrates fault-tolerance capabilities. Indeed, the continuous operation of LED lighting systems is of particular relevance in emergency lighting systems, for instance.

The majority of the proposed approaches for AEC fault diagnostics are based on monitoring the ESR and C [15]. The real-time online computational model for C and ESR estimation is solely based on the evaluation of the capacitor's ripple voltage. A condition-monitoring approach for industrial power converters is given in [5], in which an ESR estimate circuit that requires just a few op-amps, passive components, and a low-cost microcontroller is utilized. The monitoring of the electrolytic capacitor's condition in [16] is based on an assessment of its impedance at double the grid frequency (100 Hz). This method was used on a single-phase grid-connected PV system with grid power changing at double the main grid frequency. The authors of [17] describe another approach for detecting failures using ESR, C, and other parameters. Another technique for detecting capacitor aging at the output stage of a step-down DC-DC converter is suggested in [18], which is based on analyzing the output voltage dynamic response with regards to a reduction in capacitance. In [19], an on-line technique for monitoring the condition of AECs in a PV system coupled to a single-phase network is presented that involves inserting a

harmonic frequency current into the network overnight, using a solar inverter. The impedances of the capacitors are measured at various frequencies. The LMS technique is used to estimate the ESR and C values based on these impedance measurements. In [20], an innovative online C and ESR monitoring system for the output electrolytic capacitor of a DCM flyback converter is described. A non-invasive technique for estimating the output capacitor characteristics of a flyback converter is proposed in [21]. The approach suggested in [22] allows the precise determination of the capacitor's temperature. The core temperature, as well as the ESR of the capacitor, may be applied to monitor the condition of an AEC. The authors of [23] present an online fault detection technique based on a state observer mechanism, whereas [24] proposes an online ESR estimation technique for a boost converter's output capacitor, based solely on output voltage ripple and inductor current. A simple condition monitoring scheme for the sub-module capacitors of modular multilevel converters (MMC), during the estimation of the low-frequency impedance, is proposed in [25]. A disturbed voltage signal in the MMC's control loop causes a sinusoidal oscillation in the sub-module capacitor at double the operating frequency. The online condition monitoring technique presented in [3] is capable of accurately estimating the ESR_i and ESR_o, using pre-calibrated tunnel magneto-resistance (TMR) sensors. The calculation of the AC power wasted in the capacitors may be used to calculate the ESR of the electrolytic capacitors in AC–DC PWM converters [2]. In [26], on the basis of compressed sensing and the Wavelet Transform (WT), an online ESR calculation for the AECs of power electronic converters is proposed. In [27], an online monitoring method for output capacitors using the short time Fourier transform (STFT) technique in a boost converter is presented and verified. The same technique was recently used for the online condition monitoring of AECs in DC-DC interleaved boost converters (IBC), adopting a model-free predictive controller (MFPC) [28]. The short time least square Prony's (STLSP) technique was presented in [29,30] for the on-line predicting and monitoring the ESR and C for a DC-DC boost converter.

In conclusion, the condition monitoring of AECs has not previously targeted LED lighting applications. Particularly, the development of robust LED lighting systems, integrating condition-monitoring capabilities, has not been considered thoroughly in previous literature. Furthermore, most current condition-monitoring strategies evaluate single AECs, neglecting the potential interactions that may take place between multiple AECs integrated on the same converter. Furthermore, the condition-monitoring strategies described in the literature do not provide solid clues regarding their effectiveness in systems with low ratings, as is the case in LED lighting systems. The low current and voltage ratings associated with LED lighting systems, combined with the potential impact of the cross-regulation usually observed in SIMO LED drivers, pose important challenges for the effective condition monitoring of power electronics. As a result, the main goal is to deploy a reliable and cost-effective condition-monitoring system to evaluate the condition of capacitors. Emphasis is placed on the real-time estimation of the ESR and C parameters. The fault-detection task employs the STLSP method to obtain an online estimation of the ESR parameter, through a continuous evaluation of the electrolytic capacitor's condition. The STLSP technique was chosen because of its ability to properly estimate and monitor all the harmonic characteristics (frequency, amplitude, phase, and damping factor) from a short-signal recording. This is consistent with the objective of this work, as variations in ESR and C are similarly reflected in the ratio of the capacitor voltage and current ripples. This system is specifically developed for a converter architecture and a corresponding controller that ensures the continuous operation of all the LED fixtures in the presence of a capacitor fault.

1.1. Characteristics and Equivalent Circuit of AECs

AECs are made up of electrodes (one anode and one cathode), electrolytic paper, electrolytes, and an oxide layer, as seen in Figure 2 [26]. The dielectric is an oxide layer (Al_2O_3) that generates an electrochemical reaction on the electrodes' surfaces [19]. The

electrodes' surfaces are chipped to enhance the specific surface area. The fluid electrolyte, which forms the second plate of the capacitor in non-solid aluminum electrolytic capacitors, enters the pores of the anode oxide layer to give maximum surface contact and high capacitance values [15,17].
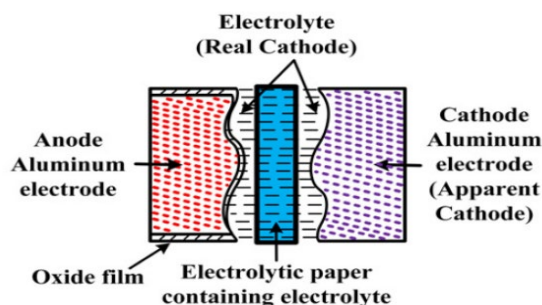

Figure 2. Structure of an aluminum electrolytic capacitor.

A capacitor is identified not just by its capacitance (C), but also by an equivalent series resistance (ESR) and an equivalent series inductance (ESL), due to its physical design and construction. Figure 3 depicts a simplified equivalent circuit of an AEC. The capacitor's internal resistance (equivalent series resistance (ESR)) is mostly caused by the resistances of the terminal, tab, foil, dielectric, electrolyte–paper, and tunnel–electrolyte. The capacitance (C) is mostly caused by the dielectric layer along the engraved tunnels, whereas the inductance is caused by the loop created by the terminals and tabs outside the winding and the inductance of the etched tunnels [5]. The ESL value is fairly small and has no meaningful effect on the total impedance. As a result, the AEC may be represented as a series combination of the ESR and the C.
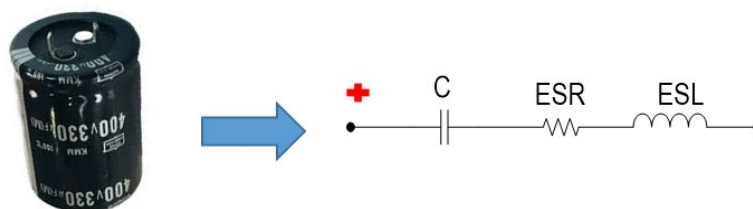

Figure 3. AEC's simplified equivalent circuit.

When the AEC is subjected to high temperatures, the electrolyte expands. The resistance decreases as the electrolyte's surface area increases. As a result, as the working temperature increases, the ESR decreases [19].

1.2. Temperature Effect

Capacitors' primary properties are typically affected by temperature, frequency, and voltage. The dielectric type and the capacitor's manufacturability have a significant impact on the temperature. Electrolytic capacitors, for example, have operating temperatures that are limited by the electrolyte rather than the dielectric. Two criteria define the lowest and maximum operating temperatures: the first is the material's resistance to the prescribed temperatures, and the second is the electrical characteristics' fluctuation range.

It is well understood that altering the operating temperature has a significant influence on the ESR and C values over time. As a result, it is critical to assess the capacitor's condition while taking temperature into consideration, especially in long-term aging studies. Typically, manufacturers set the end-of-life (EoL) limit of electrolytic capacitors when the ESR doubles and/or the capacitance decreases by 20% relative to the initial values [30].

It is crucial to note that the fluctuation in the ESR and C parameters is influenced by the severity of the defect and the operating temperature. Indeed, [2,17] represent the ESR and C parameters as functions of temperature by [2,17,31]:

$$ESR_{ref}(T) = \alpha_{ESR} + \beta_{ESR}.e^{\frac{-T}{\gamma_{ESR}}} \tag{1}$$

$$C_{ref}(T) = \alpha_C + \beta_C + \gamma_C.T^2 \tag{1}$$

where α, β, and γ are characteristic parameters of the electrolytic capacitor.

1.3. Proposed Converter Architecture

The structure of the two-output fault-tolerant LED driver and corresponding condition monitoring system is shown in Figure 4. Each light is made from individual LEDs that are wired in series.
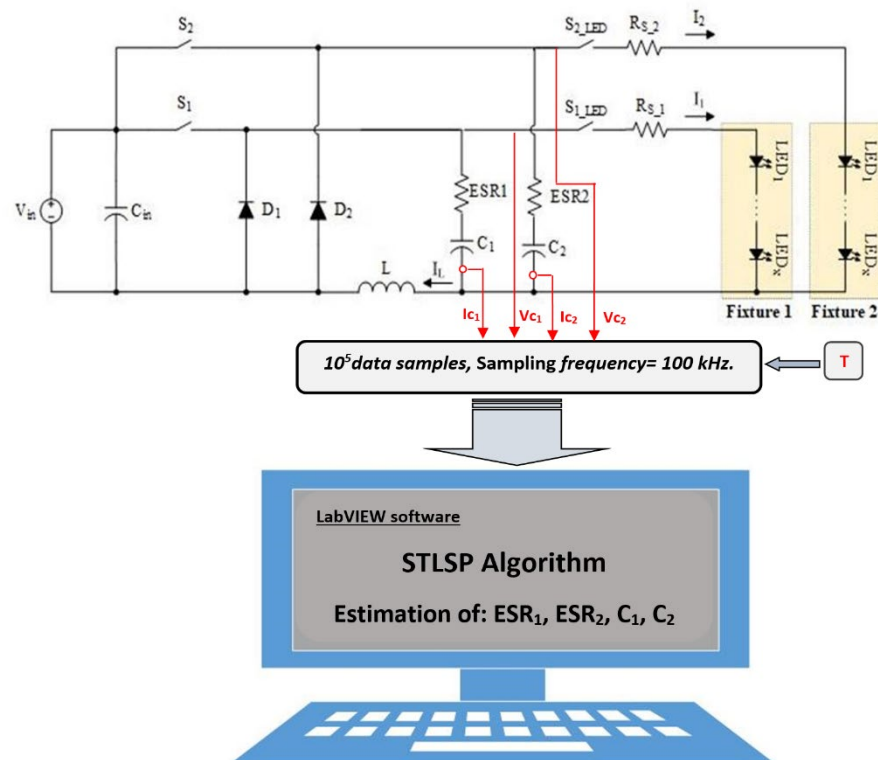

Figure 4. LED driver architecture.

The suggested architecture eliminates the need for extra components that are purely devoted to redundancy functions. If desired, the converter's extension into several outputs is substantially simplified thanks to the modular construction, allowing the connection of various LED lights.

Unlike other SIMO converters in the literature, which rely on front-end buck converters to accomplish their current control functions [32], the fault-tolerant SIMO LED driver does not [6]. A decentralized current-control function is provided by the proposed fault-tolerant converter. The front-end buck converter is removed, and current control is now handled by switches S_1 and S_2. This feature adds redundancy to a power conversion system, which is considered essential for fault tolerance. In this converter, switches S_1 and S_2

are in charge of the current control and time-sharing, while switches S_{1_LED} and S_{2_LED} perform the dimming. For enhanced control accuracy, resistors R_{S_1} and R_{S_2} translate the current flowing to the outputs into voltages, which are then used for control purposes.

2. Converter Control and Fault-Detection Algorithm

2.1. Converter Control

Accurate current control is a challenging task, particularly in fault-tolerant SIMO converters. For this reason, it is important to deploy dedicated control strategies.

Figure 5 shows a simplification of the controller adopted in the study. Note that the depicted controller solely applies for output 'n' of the converter. Accordingly, the depicted controller structure is replicated n times, in order to deploy the control functions in all the LED driver's outputs.
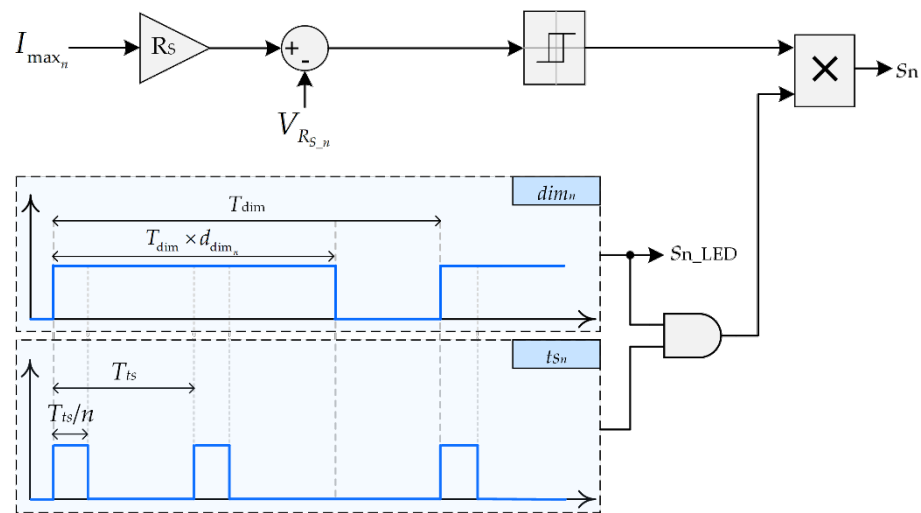

Figure 5. Converter control architecture.

The primary function of the controller comprises the accurate regulation of the individual currents flowing in each converter output. In this study, this goal is accomplished through two distinctive approaches: (1) the regulation of the ON-time current, set by the reference current for the output 'n', denoted as I_{max_n}; (2) the definition of the dimming ratio for the output 'n', denoted as d_{dim_n}. In addition to the current control, the controller also performs time-multiplexing functions, which are critical in any SIMO converter.

As shown in Figure 5, the controller generates two carrier signals internally. One of those carrier signals, termed dimming command dim_n, has a fixed frequency f_{dim} and duty ratio d_{dim_n}. The dimming frequency f_{dim} is typically low (between 300 Hz and 3 kHz). The dimming ratio d_{dim_n} is an input of the controller and is regulated to obtain the average current required to obtain the desired luminous flux for the output n. The dimming command dim_n is directly sent to the dimming switch S_{n_LED}. The other carrier signal, termed ts_n, represents the time-multiplexing function. It has a fixed frequency f_{ts} and a constant duty ratio of $1/n$, where n denotes the total number of outputs.

The current directed to each output is regulated by a dedicated control loop, based on a hysteretic controller. It compares the reference current defined for the output n (I_{max_n}) with the current observed at that output. The output of the hysteretic controller is modulated by the two carrier signals dim_n and ts_n. In practice, this means that switch S_n may only receive control commands when signal ts_n is at a high level.

2.2. Fault-Detection Algorithm

The next objective is to develop a fault-detection algorithm (FDA) that can assess the capacitor's status in real time. The FDA is based on the STLSP approach, which uses the capacitor's voltage and current ripples to estimate the capacitor's ESR online (Figure 4). The aim is to assess and monitor the ESR and C, since they provide useful indicators of the capacitor's probability of failure. The ratio between the capacitor voltage ripple and the current ripple reflects changes in the ESR and C. This ratio is equal to the impedance of the capacitor at any given time. The capacitor's impedance is dominated, in the switching frequency (f_{sw}) range, by ESR and is dominated, in the fundamental frequency (f_m) range, by C. As a consequence, ESR and C may be calculated using the following steps:

Step 01: The acquisition of the capacitors' currents and voltages $\left(V_{Cap1}, V_{Cap2}, I_{Cap1}, I_{Cap2} \right)$;

Step 02: The estimation of the magnitudes, frequencies, and phase angles related to the capacitors' currents and voltages $\left(V_{Cap1,Swt} \| V_{Cap1,fm} \| V_{Cap2,Swt} \| V_{Cap2,fm} \| I_{Cap1,Swt} \| I_{Cap1,fm} \| I_{Cap2,Swt} \| I_{Cap2,fm} \right)$.

This can be performed using the STLSP method. In this part of the approach, a high-resolution spectral analysis is deployed, based on the short time least square Prony's (STLSP) method. The STLSP is based on applying the least square Prony's method to a short-time sliding window. This technique has the ability to determine and accurately track all the attributes of the harmonics (frequency, amplitude, phase, and damping factor) from a short data record signal, which makes it possible to consider the non-stationary aspect of the problem [28]. To reduce the impact of some influential factors, and thus obtain improved accuracy, preprocessing of the acquired signal is necessary. In fact, data acquisition parameters, filtering, DC component removal, and downsampling are the main tasks involved. Among these tasks, the signal filtering is of crucial importance and directly affects the quality of the results. In this study, the capacitor current signal was acquired with a sampling frequency of 100 kHz. Next, a remarkably short sliding time window of only *n*= 30 samples was used, which represented only 0.3 *ms*.

Step 03: The estimation of the ESR and C of both capacitors, using the following conditions:

$$ESR_{C1,C2} = \frac{V_{C1,C2(fsw)}}{I_{C1,C2(fsw)}} \tag{2}$$

$$X_{C1,C2} = \frac{V_{C1,C2(fm)}}{I_{C1,C2(fm)}} \Rightarrow C_{C1,C2} = \frac{1}{2\pi fm_{(C1,C2)} \cdot X_{C1,C2}} \tag{3}$$

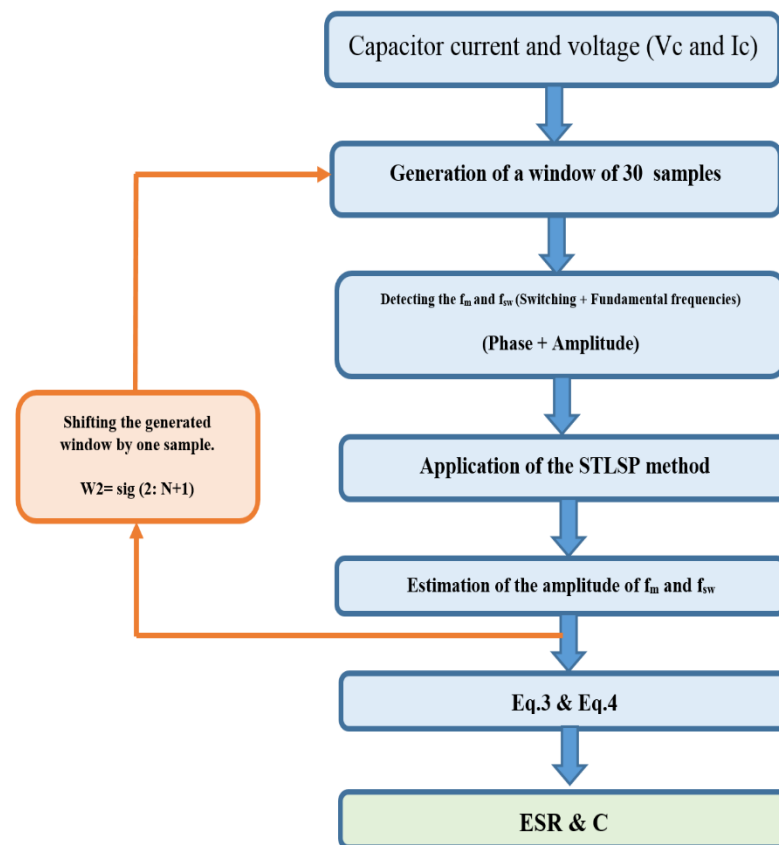Figure 6 depicts the flowchart considered in the implementation of the proposed FDA.

Figure 6. The proposed FDA.

3. Experimental Results

Figure 7 depicts the experimental setup used to test the effectiveness of the suggested fault-tolerant LED lighting system and corresponding FDA. The suggested LED driver and fault-tolerant modulation schemes were tested in order to determine their performance. The converter components' parameters are compiled in Table 1.
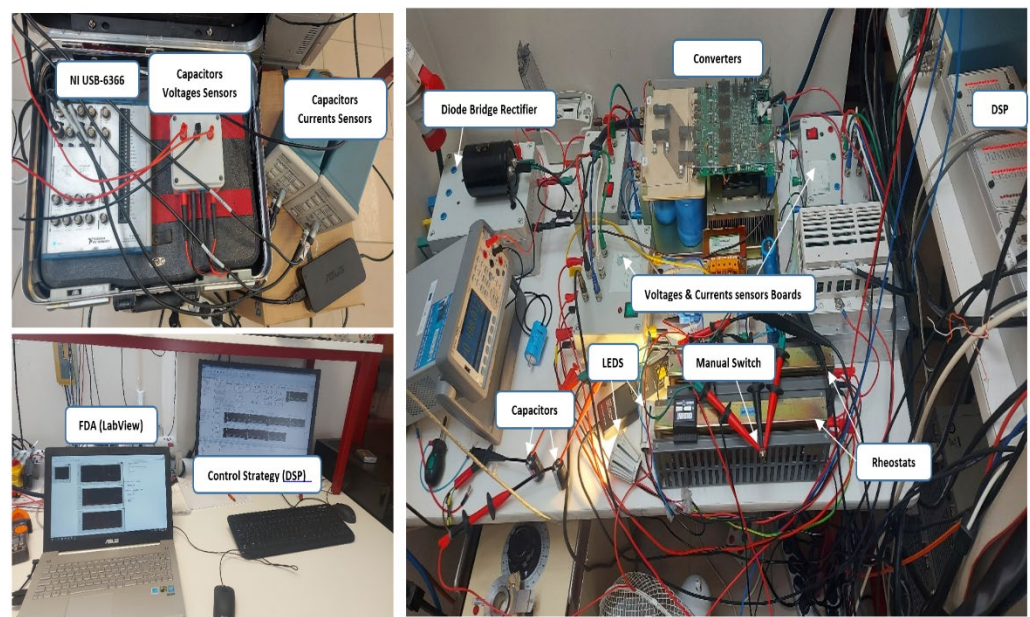

Figure 7. Fault-tolerant LED lighting system integrating the proposed FDA.

Table 1. Experimental test bench parameters.

Parameter	Nomenclature	Value
Input voltage	V_{in}	200 V
Inductance	L	10 mH
Capacitance	$C_{1...n}$	220 μF
No. of LEDs per fixture (connected in series)	m	15
No. of LED fixtures	n	2
LED fixture nominal voltage	$V_{n_{nom}}$	48 V
LED fixture nominal current	$I_{n_{nom}}$	0.22 A
LED fixture nominal power	$P_{n_{nom}}$	11 W
Time-sharing frequency	f_t	5 kHz
Dimming frequency	f_{dim}	600 Hz

The software component implemented in the experimental procedures is composed of two parts:

- Control part, performed by the dSPACE DS1103 board, operating with a sampling time of 25 μs.
- Fault-detection part, performed by the acquisition card, using LabVIEW.

The objective was to examine the dynamic behavior of the system and show the resilience of the proposed controller and FDA in various operating modes, including degraded operation conditions. Even if certain converter components were to fail, the optimal technique for operating the converter was expected to maintain complete dynamic and tracking performance. Hence, the dependability of the proposed controller was tested in the face of a capacitor defect. The challenge was to detect the presence of a capacitor defect while ensuring that the system's dynamics and tracking performance were unaffected. A FDA was deployed in parallel with the controller to address this challenge. As previously indicated, the proposed FDA computes and tracks the ESR and C parameter, using the capacitors' currents and voltages as inputs.

On the output side, the adopted LED driver essentially consists of two electrolytic capacitors, as the developed LED lighting system integrates two outputs. To introduce the capacitor fault in each output, another faulty capacitor was connected in parallel to the original capacitor—the healthy one—to simulate a capacitor failure. The commutation between the healthy and faulty capacitors was controlled by a bidirectional switch.

To create a defective capacitor, a healthy electrolytic capacitor was placed in a temperature-controlled oven, at 200 °C, for 4 h, to accelerate the aging process. The ESR and C properties of both healthy and defective capacitors were tested with a precision RLC meter, set to measure at the switching frequency (5005 Hz) and at the fundamental frequency (590 Hz). The acquired ESR and C values are shown in Table 2.

Table 2. The measured ESR and C.

	Cap1	Cap2	Faulty Cap
ESR (Ω)	0.2128	0.2209	0.8500
C (μF)	209.41	208.87	185.80

The acquisition of the capacitor's voltage and current signals started when the proposed system was functioning with a healthy electrolytic capacitor. The bidirectional switch was commutated to the aged capacitor after a few seconds. Figure 8 depicts the instantaneous LED fixture currents for three distinctive operating scenarios: (1) healthy condition; (2) faulty Cap1; (3) faulty Cap2. Regardless of the capacitor condition, the ef-

fective regulation of the outputs' currents was achieved, with minimal impact on the harmonic content. Therefore, even in the case of a capacitor defect, the suggested controller is capable of sustaining effective current control.
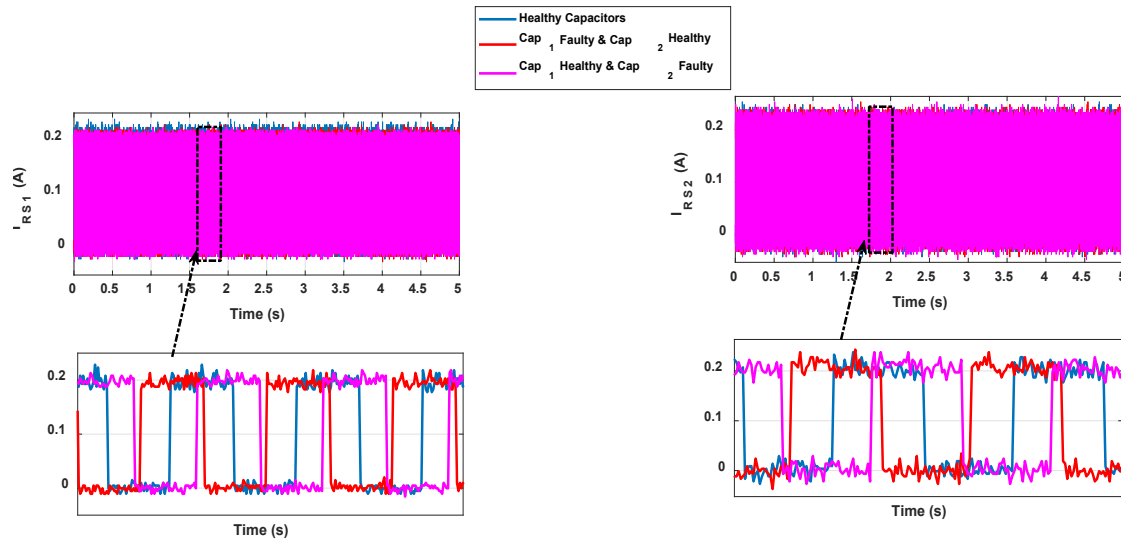

Figure 8. LED fixtures' instantaneous currents I_{Rs1} and I_{Rs2}, considering both states (healthy and faulty).

Figure 9 provides a broader view of the LED fixtures' instantaneous currents I_{Rs1} and I_{Rs2}, embracing the healthy operation and the transient-to-faulty operation of Cap1 and Cap2. Compared with I_{Rs1}, I_{Rs2} was affected a little more by the presence of the fault in Cap2.
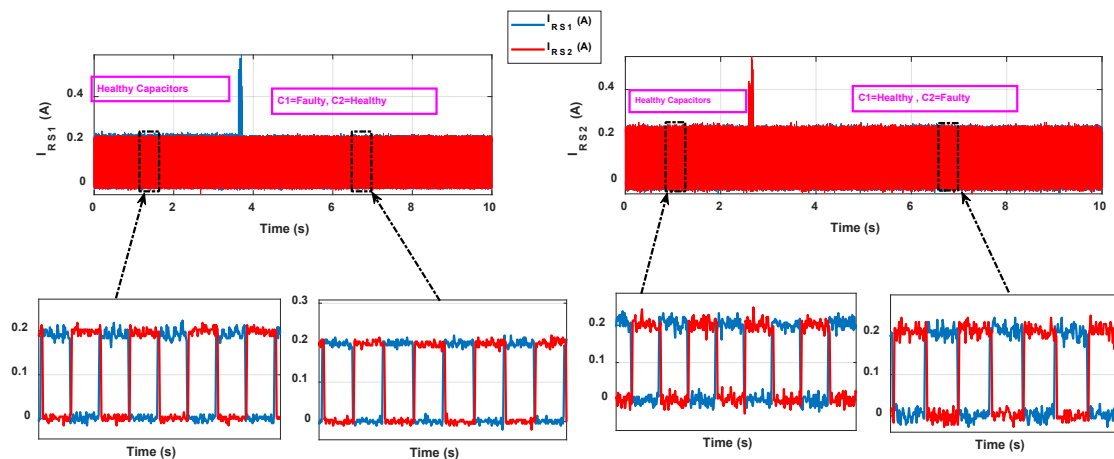

Figure 9. LED fixtures' instantaneous currents I_{Rs1} and I_{Rs2}, showing the fault transience in the two capacitors (Cap1 and Cap2).

The proposed FDA requires the capacitor's voltage and current signals, obtained with an NI USB-6366 data acquisition card. For data acquisition, the sampling rate was set at 100 kHz. The STLSP method was developed in MATLAB code and placed into the LabVIEW program, through the MATLAB script node, for the online execution of the suggested FDA. The other steps in the proposed method, such as low-pass filtering and downsampling, were performed directly using the LabVIEW palettes.

The converter was configured such that the system's output voltages, observed at the capacitors, tracked the reference voltage regardless of internal disturbances (for example, parametric variation or converter malfunction) or external disturbances (variation in load, temperature, etc.). The experimental results depicted in Figure 10 show that the output voltage, measured in both capacitors (Cap1 and Cap2), remained unaffected by the occurrence of the fault in the capacitors. Figure 10 clearly shows that there were no meaningful changes in the capacitor's voltage waveforms after the occurrence of the capacitor fault. On the other hand, significant variations were noticed in different spectral components of the capacitors' voltages and currents, as shown in the Figure 11.
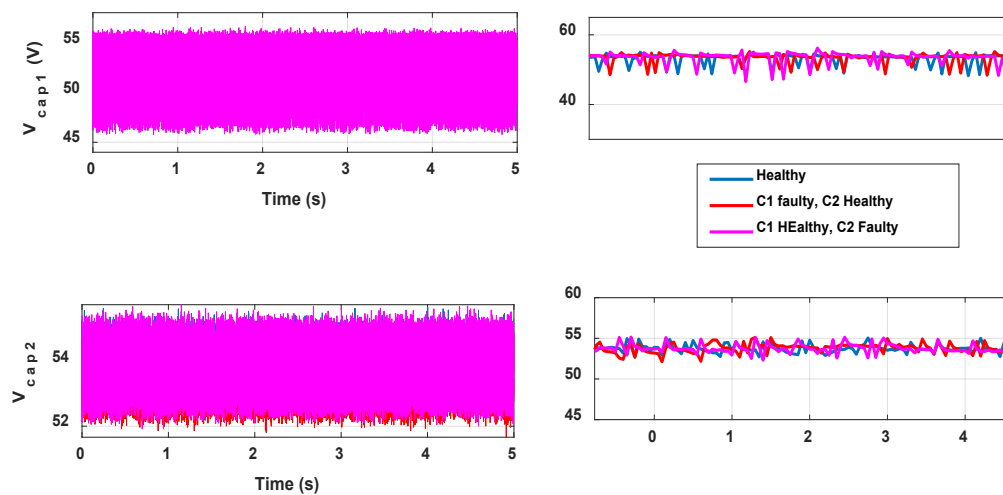

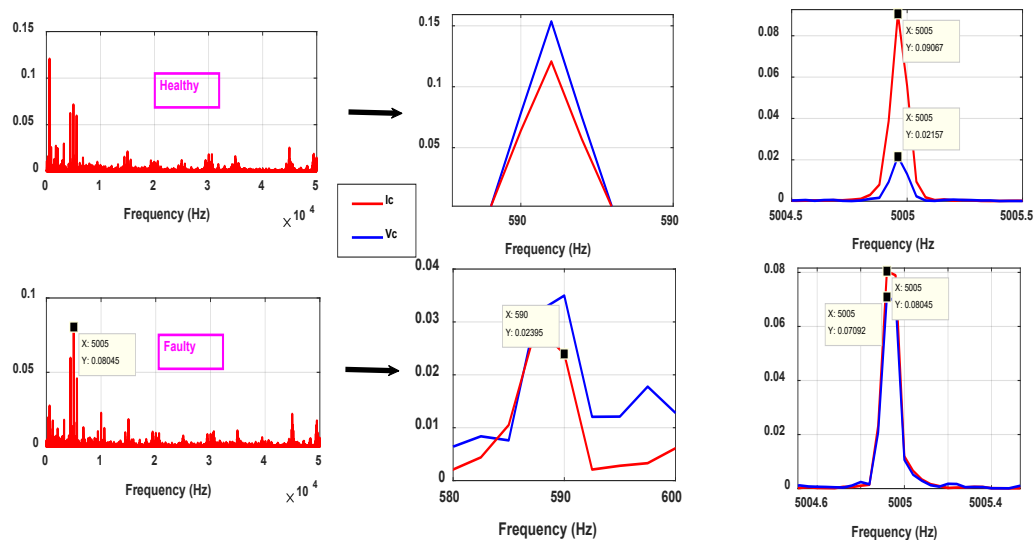**Figure 10.** Cap1 and Cap2 voltage in healthy and faulty states.

**Figure 11.** Voltage and current spectra of Cap1 in both states (healthy and faulty).

Figure 11 illustrates the spectra of the capacitors' voltages and currents, assessed in both states (healthy and faulty). The estimations of the ESR and C parameters, computed through the proposed STLSP algorithm, are compiled in Table 3.

Table 3. Estimated ESR and C values for Cap1 and Cap2 (healthy capacitors) and Cap1 (faulty capacitor).

	Healthy				Faulty	
	Cap1	Cap2	Error (%)		Cap1	Error (%)
			Cap1	Cap2		
ESR (Ω)	0.221	0.232	3.69	4.80	0.8775	2.13
C (μF)	212.15	212.35	1.29	1.64	189.1	1.73

It should be noted that the accurate definition of the FFT spectrum, obtained by traditional methods, requires at least n = 20,000 samples, obtained in the stationary regime. In turn, the proposed STLSP algorithm enables the on-line and highly accurate estimation of the spectral distribution, with just n = 30 samples.

Figures 12 and 13 show the online estimation of the ESR and C parameters, observed when Cap1, which was initially healthy, was replaced by the faulty capacitor. Before the occurrence of the capacitor fault, the mean values of the estimated ESR and C for Cap1 were equal to 0.221 Ω and 212.15 µF, respectively. Compared with the values given by the RLC meter, the relative errors were 3.69% and 1.29%, respectively. For Cap2, the mean values of the estimated ESR and C were equal to 0.232 Ω and 212.35 µF, respectively. Compared with the values given by the RLC meter, the relative errors were 4.8% and 1.637%, respectively. After switching Cap1 to the aged capacitor, the ESR increased considerably, whereas the capacitance decreased. These observations are in agreement with the theoretical predictions. The time-domain representation of the estimated ESR and C values shows that, after a short transitional period, the estimations of the ESR and C for Cap1 converged to the new mean values of 0.8775 Ω and 189.1 µF, respectively, which corresponded to the following relative errors: 2.13% and 1.73%. The obtained results demonstrate that the proposed method was able to successfully estimate and accurately track the electrolytic capacitor parameters, even under highly distorted signals, low voltage and current ratings, and non-stationary operating conditions.
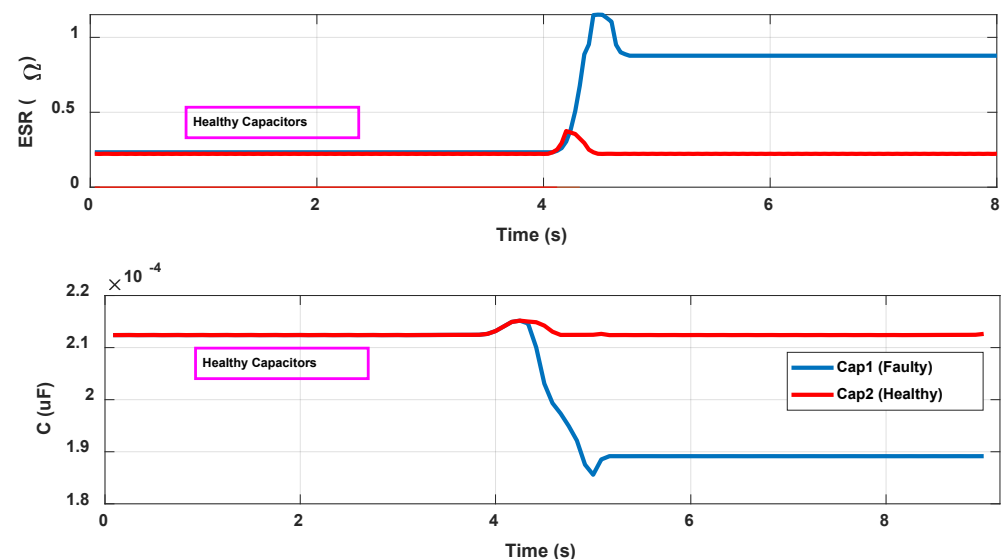
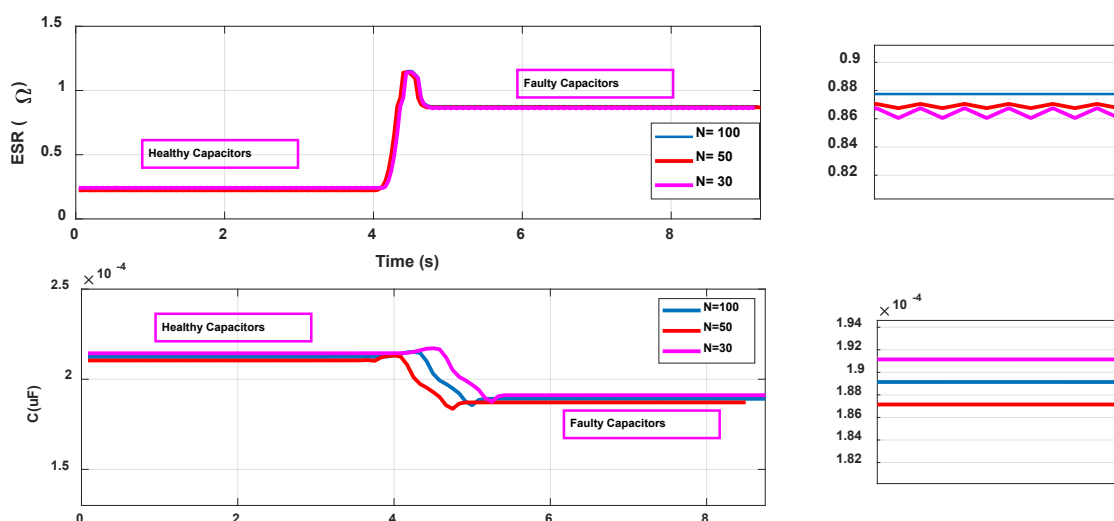**Figure 12.** Estimated ESR and C in both states (healthy and faulty).

Figure 13. Estimated ESR and C in both states (healthy and faulty) as a function of the number of data samples N.

Effect of the Number of Treated Samples

To evaluate the electrolytic capacitor's condition, the STLSP approach was utilized to determine the ESR parameters and C. Since the algorithm implies the inversion of large-size matrices and operations with high-order polynomials, examining the algorithm's computing cost is important. The number of treated data samples N has a significant impact on the complexity involved.

For this context, tests were performed with different values of N (number of treated samples) to show the effectiveness of the proposed technique, even at reduced N. The estimated values of the ESR and C are shown in Table 4.

Table 4. Estimated ESR and C at different values of N.

Number of Treated Samples (N)	30	50	100
ESR (Ω)	0.2309	0.228	0.221
Error (%)	5.01	4.59	1.36
C (μF)	213.7	213	212.4
Error (%)	2.05	1.71	1.43

Figure 13 shows the estimated ESR and C for Cap1—the capacitor affected by a fault—for the operating conditions considered in Figure 12. It demonstrates how the estimations of the ESR and C were affected by the number of data samples N. The results shown in Figure 13 reveal that the proposed fault detection algorithm is well suited for condition-monitoring applications, especially noninvasive defect-identification approaches. Furthermore, the STLSP technique, which is at the core of the proposed algorithm, can manage noisy and nonstationary data while remaining unaffected by system parameter changes. Discrete Fourier transform (DFT), the root of multiple approaches considered in the literature, solely provides information on the amplitudes and frequencies of the necessary harmonics, even with an extended signal record. Furthermore, DFT is unable to monitor harmonic features in any way.

4. Conclusions

In this paper, a novel fault-detection algorithm was suggested and its implementation on a LED lighting system integrating fault tolerance capabilities was described. The proposed LED driver guarantees uninterrupted supply to all the LED fixtures and consequent resilience against capacitor failures. The FDA uses the short time least square Prony (STLSP) approach to estimate the ESR and C parameters in real time, enabling the continuous evaluation of the electrolytic capacitor status based on simple electrical characteristics. Compared to existing methods, the main advantages of the proposed work are as follows:

- The proposed calculation of the AECs' parameters is simple, and it is inductance-independent.
- The proposed method can be applied in both AC-DC and DC-DC conversion schemes.
- The results show the ability of the proposed STLSP method to continuously evaluate the electrolytic capacitor state, with an estimation accuracy almost equal to 5%, which allows the detection of potential capacitor faults and, consequently, the avoidance of total system failure.
- The ability to predict the ESR and C is unaffected by the number of processed data samples N.
- The adopted fault-tolerant LED driver architecture has no effect on the performance of the proposed fault diagnosis technique.

Reference

1. Zhao, Z.; Davari, P.; Lu, W.; Wang, H.; Blaabjerg, F. An Overview of Condition Monitoring Techniques for Capacitors in DC-Link Applications. *IEEE Trans. Power Electron.* **2021**, *36*, 3692–3716.
2. Wu, Y.; Du, X. A VEN Condition Monitoring Method of DC-Link Capacitors for Power Converters. *IEEE Trans. Ind. Electron.* **2019**, *66*, 1296–1306.
3. Miao, W.; Liu, X.; Lam, K.H.; Pong, P.W.T. Condition Monitoring of Electrolytic Capacitors in Boost Converters by Magnetic Sensors. *IEEE Sens. J.* **2019**, *19*, 10393–10402.
4. Sundararajan, P.; Sathik, M.H.M.; Sasongko, F.; Tan, C.S.; Tariq, M.; Simanjorang, R. Online Condition Monitoring System for DC-Link Capacitor in Industrial Power Converters. *IEEE Trans. Ind. Appl.* **2018**, *54*, 4775–4785.
5. Amaral, A.M.R.; Cardoso, A.J.M. On-line fault detection of aluminium electrolytic capacitors, in step-down DC–DC converters, using input current and output voltage ripple. *IET Power Electron.* **2012**, *5*, 315–322.
6. Bento, F.; Cardoso, A.J.M. Fault-Tolerant LED Lighting Systems Featuring Minimal Loss of Luminous Flux. *IEEE IEEE Trans. Ind. Appl.* **2020**, *56*, 4309–4318.
7. Bento, F.; Cardoso, A.J.M. Comprehensive survey and critical evaluation of the performance of state-of-the-art LED drivers for lighting systems. *Chin. J. Electr. Eng.* **2021**, *7*, 21–36.
8. Patterson, B.T. DC, come home: DC microgrids and the birth of the "enernet". *IEEE Power Energy Mag.* **2012**, *10*, 60–69.

9.   Yang, W.-H.; Yang, H.-A.; Huang, C.-J.; Chen, K.-H.; Lin, Y.-H. A High-Efficiency Single-Inductor Multiple-Output Buck-Type LED Driver With Average Current Correction Technique. *IEEE Trans. Power Electron.* **2018**, *33*, 3375–3385.

10. Cheng, H.L.; Chang, Y.N.; Yen, H.C.; Hua, C.C.; Su, P.S. An Interleaved Flyback-Typed LED Driver with ZVS and Energy Recovery of Leakage Inductance. *IEEE Trans. Power Electron.* **2019**, *34*, 4497–4508.

11. Zhou, R.; Yeung, R.S.C.; Chan, J.Y.C.; Tse, N.C.F.; Chung, H.S.H. Switched-Capacitor-Based Current Compensator for Mitigating the Effect of Long Cable between PWM Driver and LED Light Source. *IEEE Trans. Power Electron.* **2018**, *33*, 6171–6186.

12. Menke, M.F.; Duranti, J.P.; Roggia, L.; Bisogno, F.E.; Tambara, R.V.; Seidel, Á.R. Analysis and Design of the LLC LED Driver Based on State-Space Representation Direct Time-Domain Solution. *IEEE Trans. Power Electron.* **2020**, *35*, 12686–12701.

13. Zeng, J.; Liu, F.; Liu, J.; Cheng, K.W.E. A Flexible Mode Electrolytic Capacitor-Free LED Driver With High Efficiency Over a Wide Range of Input Voltage. *IEEE Trans. Power Electron.* **2020**, *35*, 8490–8500.

14. Liu, X.; Li, X.; Zhou, Q.; Xu, J. Flicker-Free Single Switch Multi-String LED Driver With High Power Factor and Current Balancing. *IEEE Trans. Power Electron.* **2019**, *34*, 6747–6759.

15. Yu, Y.; Zhou, T.; Zhu, M.; Xu, D. Fault diagnosis and life prediction of dc-link aluminum electrolytic capacitors used in three-phase ac/dc/ac converters. In Proceedings of the 2012 Second International Conference on Instrumentation, Measurement, Computer, Communication and Control, Harbin, China, 8–10 December 2012; pp. 825–830.

16. Ahmad, M.W.; Agarwal, N.; Kumar, P.N.; Anand, S. Low-Frequency Impedance Monitoring and Corresponding Failure Criteria for Aluminum Electrolytic Capacitors. *IEEE Trans. Power Electron.* **2017**, *64*, 5657–5666.

17. Amaral, A.M.R.; Cardoso, A.J.M. A Simple Offline Technique for Evaluating the Condition of Aluminum–Electrolytic–Capacitors. *IEEE Trans. Ind. Electron.* **2009**, *56*, 3230–3237.

18. Hannonen, J.; Honkanen, J.; Ström, J.P.; Kärkkäinen, T.; Räisänen, S.; Silventoinen, P. Capacitor Aging Detection in a DC–DC Converter Output Stage. *IEEE Trans. Ind. Appl.* **2016**, *52*, 3224–3233.

19. Agarwal, N.; Ahmad, M.W.; Anand, S. Quasi-Online Technique for Health Monitoring of Capacitor in Single-Phase Solar Inverter. *IEEE Trans. Power Electron.* **2017**, *33*, 5283–5291.

20. Yao, K., Li, H., Li, L., Guan, C., Li, L., Zhang, Z.; Chen, J. A Noninvasive Online Monitoring Method of Output Capacitor's C and ESR for DCM Flyback Converter. *IEEE Trans. Power Electron.* **2018**, *34*, 5748–5763.

21. Yao, K.; Cao, C.; Yang, S. Noninvasive Online Condition Monitoring of Output Capacitor's ESR and C for a Flyback Converter. *IEEE Trans. Instrum. Meas.* **2017**, *66*, 3190–3199.

22. Prasanth, S., Halick, M., Sathik, M., Sasongko, F., Seng, T.C., Yaxin, P.; Simanjorang, R. Condition Monitoring of Electrolytic Capacitor based on ESR Estimation and Thermal Impedance model using Improved Power Loss Computation. In Proceedings of the 2018 International Power Electronics Conference (IPEC-Niigata 2018-ECCE Asia), Niigata, Japan, 20–24 May 2018; pp. 416–421.

23. Meng, J.; Chen, E.-X.; Ge, S.-J. Online E-Cap Condition Monitoring Method Based on State Observer. In Proceedings of the 2018 IEEE International Power Electronics and Application Conference and Exposition (PEAC), Shenzhen, China, 4–7 November 2018; pp. 1–6.

24. Ren, L.; Gong, C.; Zhao, Y. An Online ESR Estimation Method for Output Capacitor of Boost Converter. *IEEE Trans. Power Electron.* **2019**, *34*, 10153–10165.

25. Ronanki, D.; Williamson, S.S. Quasi-Online Low-Frequency Impedance Monitoring Scheme for Submodule Capacitors in Modular Multilevel Converters. In Proceedings of the 2019 IEEE Applied Power Electronics Conference and Exposition (APEC), Anaheim, CA, USA, 17–21 March 2019; pp. 83–90.

26. Li, C.; Yu, Y.; Yang, Z.; Liu, Q.; Peng, X. ESR Estimation for Aluminum Electrolytic Capacitor of Power Electronic Converter Based on Compressed Sensing and Wavelet Transform. *IEEE Trans. Ind. Electron.* **2021**, *69*, 1948–1957.

27. Laadjal, K.; Sahraoui, M.; Cardoso, A.J.M. On-Line Fault Diagnosis of DC-Link Electrolytic Capacitors in Boost Converters Using the STFT Technique. *IEEE Trans. Power Electron.* **2021**, *36*, 6303–6312.

28. Laadjal, K.; Bento, F.; Jlassi, I.; Cardoso, A.J.M. Online Condition Monitoring of Electrolytic Capacitors in DC-DC Interleaved Boost Converters, Adopting a Model-Free Predictive Controller. In Proceedings of the 2021 IEEE 15th International Conference on Compatibility, Power Electronics and Power Engineering (CPE-POWERENG), Florence, Italy, 14–16 July 2021; pp. 1–6.

29. Laadjal, K.; Sahraoui, M.; Cardoso, A.J.M.; Amaral, A.M.R. Online Estimation of Aluminum Electrolytic-Capacitor Parameters Using a Modified Prony's Method. *IEEE Trans. Ind. Appl.* **2018**, *54*, 4764–4774.

30. Cardoso, A.J.M. *Diagnosis and Fault Tolerance of Electrical Machines*, *Power Electron. Drives*; The Institution of Engineering and Technology (IET): Futures Place, Kings Way, Stevenage, London, UK, (ISBN: 978-1-78561-531-3), 2018.

31. Ahmad, M.W.; Agarwal, N.; Anand, S. Online Monitoring Technique for Aluminum Electrolytic Capacitor in Solar PV-Based DC System. *IEEE Trans. Ind. Electron.* **2016**, *63*, 7059–7066.

32. Li, S.; Guo, Y.; Tan, S.C.; Hui, S.Y.R. An Off-line Single-Inductor Multiple-Output LED Driver with High Dimming Precision and Full Dimming Range. *IEEE Trans. Power Electron.* **2017**, *32*, 4716–4727.